CrossMark

Manufacturing, Structure Control, and Functional Testing of Ti–Nb-Based SMA for Medical Application

S. Prokoshkin[1] · V. Brailovski[2] · S. Dubinskiy[1] · Y. Zhukova[1] · V. Sheremetyev[1] ·
A. Konopatsky[1] · K. Inaekyan[2]

Abstract This paper focuses on the development and characterization of Ni-free shape memory alloys, more specifically, Ti–Nb-based alloys for biomedical applications. It starts by describing the smelting technology used to produce small and medium size ingots of selected compositions. Thermomechanical treatments: structure interrelations are discussed next. Finally, the results of their mechanical, electrochemical, and in vitro cytotoxicity testing are presented to allow a general assessment of the mechanical, chemical, and biological aspects of compatibility of these alloys, and of the methods to control their functional properties.

Keywords Biocompatibility · Aging · Fatigue · Mechanical behavior · Superelasticity · Thermomechanical treatment · Ni-free

Introduction

Two main aspects of biocompatibility should be taken into consideration when developing new load-bearing biomaterials: biomechanical compatibility and biochemical compatibility. Biomechanical compatibility, also known as "bulk compatibility", requires that the mechanical behavior of the material be as close as possible to that of living tissues. Biochemical compatibility, also known as "interface compatibility", implies high chemical and electrochemical corrosion resistance of the material in body fluids, and the absence of an adverse material interaction with the biological environments, including the absence of cytotoxicity and mutagenicity. To develop a material combining bulk and interfacial biocompatibilities, it is necessary not only to select the material composition, but also to optimize its processing conditions, since the same processing sequence can be beneficial for the bulk compatibility while being detrimental for the interface compatibility, and vice versa.

Titanium nickelide-based shape memory alloys (SMAs) are often regarded as excellent candidates for medical implants because they combine low-stiffness superelastic behavior with high mechanical and corrosion resistance in body fluids [1–8]. Moreover, if specific polygonizing or nanostructuring thermomechanical treatments (TMTs) are applied to these alloys, their functional characteristics approach their theoretical limits [9–30]. The only negative feature of Ti–Ni-based SMAs is the presence of toxic nickel in their composition, which is a factor of risk for any permanent or long-term implant application. This specificity of Ti–Ni alloys has triggered intensive research activities aimed at developing nickel-free SMAs [7, 31–42]. The design of multi-component Ti–Nb- and Ti–Zr-based SMAs has become one of the targets of these fundamental and applied investigations.

Following this objective, a series of collaborative studies on Ti–Nb–Zr and Ti–Nb–Ta SMAs have recently been carried out at the National University of Science and Technology "MISIS" (Moscow, Russia) and Ecole de technologie superieure (Montreal, Canada). These investigations were focused on the following topics [43–57]:

✉ S. Prokoshkin
  prokoshkin@tmo.misis.ru

1   National University of Science and Technology "MISIS",
    Leninskiy prosp. 4, Moscow, Russia 119049

2   Ecole de technologie superieure, 1100, Notre-Dame Str.
    West, Montreal, QC H3C 1K3, Canada

(1) Development of the small and medium size Ti–Nb–Zr and Ti–Nb–Ta ingots' production via the smelting technology;

(2) Study of the TMT: grain/subgrain structure interrelations in the selected alloys;

(3) Functional mechanical characterization of the TMT-processed alloys, including: (a) static mechanical characterization, (b) long-term stability testing, and (c) elastic/superelastic fatigue testing;

(4) Biochemical compatibility characterization of the TMT-processed alloys including: (a) electrochemical corrosion testing in simulated body fluids, and (b) in vitro cytotoxicity testing.

Some selected results of these investigations are described and discussed below in the same order as presented above, to allow a general assessment of the main aspects of biocompatibility of the Ti–Nb–Zr and Ti–Nb–Ta alloys and of the methods to control their functional properties.

Experimental Procedure

Materials Production and Processing

Before starting the manufacturing procedure, the melting points of the studied Ti–Nb–Zr and Ti–Nb–Ta alloys were calculated (see "Appendix" section; note that the alloys' compositions are given in at.% throughout this work).

Small size ($\sim$200 g) Ti–Nb- and Ti–Zr-based alloys' ingots for preliminary testing were smelted using a custom-made laboratory vacuum arc furnace with a non-consumable tungsten electrode under argon atmosphere. The procedure included several remelting steps.

Medium size 50 mm diameter, 660-mm-long Ti–21.8Nb–6Zr ingots were produced by *Flowserve Corp.* (USA) via induction skull melting and isostatic pressing (900 °C, 100 MPa, 120 min). In parallel to that, in collaboration with *The I.P. Bardin Central Research Institute for Ferrous Metallurgy* (*CRIFM*, Russia), the vacuum arc melting (VAM) technique with consumable electrode was applied to produce medium size Ti–Nb-based alloys' ingots. 350-mm-long (Ti–19.7Nb–5.8Ta) and 150-mm-long (Ti–22Nb–6Zr) 80 mm diameter ingots were then produced, hot-forged at 900 °C, and machined to a 50 mm diameter. The procedure included several remelting steps, starting from a consumable electrode containing high-purity raw materials (Ti, Nb, Ta/Zr).

It should be noted that scaling up from small size to medium size ingots is a necessary step for the full-scale characterization of prospective alloys and for the production of these alloys in powder form via the atomization technique [3].

Ti–21.8Nb–6Zr and Ti–19.7Nb–5.8Ta 1×1 and 2×10 mm cross-section tensile testing specimens with different gauge lengths, and $5 \times 10 \times 20$ and $1 \times 5 \times 5$ mm plate specimens for long-term corrosion and in vitro testing were EDM-cut from the ingots. All the specimens were subjected to TMT comprising cold rolling (CR) with moderate true strain ($e = 0.3$–0.37), followed by post-deformation annealing (PDA) in the 450,…,750 °C temperature range (15, …,60 min) and subsequent water cooling. Additional age-hardening (AG) at 300 °C from 15 to 180 min with subsequent water cooling was optionally performed on selected alloys. For electrochemical testing, 0.5 mm diameter Ti–19.7Nb–5.8Ta and Ti–22Nb–6Zr wire specimens were produced by multi-pass cold drawing with inter-pass annealing at 600 °C for 10 min.

Characterization

The chemical composition homogeneity of the obtained ingots was studied using a *JEOL JSM-6700* scanning electron microscope (SEM) with a *JED-2300F* X-ray microanalysis attachment.

Structure evaluation was performed using a *JEOL 2100* transmission electron microscope (TEM). TEM samples were mechanically grinded and polished down to a 0.1 mm thickness. The final electrochemical polishing was performed at −38 °C in 15 % HNO_3 spirit solution using a *Tenupol-5* system (*Struers*, Denmark).

The evaluation of the mechanical and functional properties of the alloys was performed at room temperature (RT) with a 0.02 s^{-1} strain rate using an *MTS MiniBionix* testing machine and three testing modes:

(1) *Superelastic testing* multi-cycle isothermal tensile testing with 2 % constant strain per cycle to specimen failure (80 mm gauge-length specimens).

(2) *Functional long-term stability evaluation combining* first series of 10-cycle 2 % strain loading–unloading tensile testing, 40-day pause, second series of 10-cycle testing, 365-day pause, and third series of 10-cycle testing (30 mm gauge-length specimens).

(3) *Functional fatigue testing* tensile strain-controlled fatigue testing. The following strains were applied: 0.2, 0.3, 0.5, 0.7, 1.0, and 1.5 %. For each level of strain, three specimens were tested. All the fatigue tests were carried out either to specimen failure or up to a maximum preset number of cycles (run-out at 10^6 cycles) (80 mm gauge-length specimens).

Corrosion and electrochemical studies were carried out at 37 ± 1 °C in Hank's solution imitating inorganic components of the osseous tissue and containing (concentrations, g/l): 8 NaCl, 0.4 KCl, 0.12 $Na_2HPO_4 \cdot 12H_2O$, 0.06 KH_2PO_4, 0.2 $MgSO_4 \cdot 7H_2O$, 0.35 $NaHCO_3$, 0.14 $CaCl_2$,

H_2O (up to 1 l of solution), pH 7.4. These studies involved the following tests:

(1) *Long-term corrosion testing* these tests were carried out with the full immersion of the specimens for 3 months. Metallic ion concentrations were measured using an *iCAP 6300 Radial View* atomic emission spectroscopy with inductively coupled plasma ($5 \times 10 \times 20$ mm specimens).

(2) *Electrochemical testing* open circuit potential (OCP) and polarization diagram measurements were carried out using two- or three-electrode cells with divided electrode space and an *IPC micro* electronic potentiostat. A saturated silver/silver chloride electrode and platinum electrode were used as the reference and auxiliary electrodes, respectively ($1 \times 10 \times 15$ mm specimens).

(3) *Electrochemical testing under cyclic load* 0.1–1.5 % strains were applied to the immerged specimens using an originally designed experimental setup [57]. The setup allowed direct loading of the specimens placed in test media with a 1 Hz cycling frequency; most of the strain values were characteristic of an intraosseous implant's in vivo performance conditions (0.5 mm diameter, 80-mm-long wire specimens).

In vitro cell survival studies were performed using 3-(4,5-dimethylthiazol-2-yl)-2,5-diphenyltetrazolium bromide (MTT) colorimetric testing on human fibroblast cells incubated in Eagle's medium at 37 °C. After 2 days of incubation in a microplate, the culture medium was extracted from the wells and 1 ml of the medium with 200 μl of MTT (*Sigma*) with an initial concentration of 5 mg/ml was added; the incubation was performed for 1 day. The medium with MTT was then removed and 1 ml of dimethyl sulfoxide was added to dissolve the formazan crystals that had formed. The cell precipitate was resuspended for 5 min by pipetting. Cell viability was estimated by the solution color intensity, which was characterized by its optical density at a wavelength of 545 nm using an *Immunochem 2100* photometer. The calculation of the number of the grown cells, and of their size and volume was carried out using a manual automated cell counter *Scepter Millipore* pipette which enabled the cell concentration, size, and volume distribution to be obtained. Fibroblast incubation was carried out for 4 days. Next, the monolayer of the cells grown on the bottom of the wells was studied by optical microscopy (*Olympus CKX41*), removed by 0.02 % Versene solution with 0.1 mg/ml chymopsin, and diluted in 1 ml of Eagle's medium to enable *Scepter Millipore* pipette counting ($1 \times 5 \times 5$ mm specimens were used).

Experimental Results

Manufacturing Ti–Nb- and Ti–Zr-Based SMAs

Small Size Ingots

It was shown that it takes three sequential remelting steps to produce homogeneous 180 g ingots of Ti–22Nb–6Zr, while it takes at least four remelting steps to produce homogeneous 166 g ingots of Ti–22Nb–6Ta. Figure 1 shows the element distribution maps obtained for these alloys (SEM). The dark areas in the Ti and Nb element maps and the bright areas in the Ta map correspond to the grinding after-effect. (In our case, SiC paper was used and Si peaks are very close to Ta peaks.) Integral chemical compositions were as follows: Ti–22.1Nb–6.0Zr and Ti–22.4Nb–4.6Ta.

Medium Size Ingots

It was shown that after first remelting, the *CRIFM's* medium size Ti–Nb–Ta ingot was visibly inhomogeneous, with visible Ta-rich spots (Fig. 2).

After the second remelting, the homogeneity of the ingot was improved, but it still featured some Ta-rich inclusions and significant differences between the actual and the target compositions of the surrounding solid solution matrix (average composition Ti–25.0Nb–1.3Ta). The observed ingot's inhomogeneity and compositional mismatch were mainly due to the proximity of the Ta melting temperature, which is above 3000 °C, to the temperature of intensive evaporation of Ti.

An alternative way to produce such ingots involved the smelting of a foundry alloy (Nb–Ta), whose melting temperature was lower than that of pure Ta ($\sim$2600 °C compared to $\sim$3000 °C). This alloy was further remelted with Ti to obtain the final ingot. SEM images of the bottom and top ingot parts are given in Fig. 3. The corresponding chemical compositions are listed in Table 1.

It can be observed that only the bottom part of the ingot can be considered homogenous, and consequently, appropriate for further processing. At the same time, medium size Ti–22Nb–6Zr ingots with post-melting processing similar to that of their Ti–Nb–Ta counterparts appeared to be much easier to produce, since after the second remelting
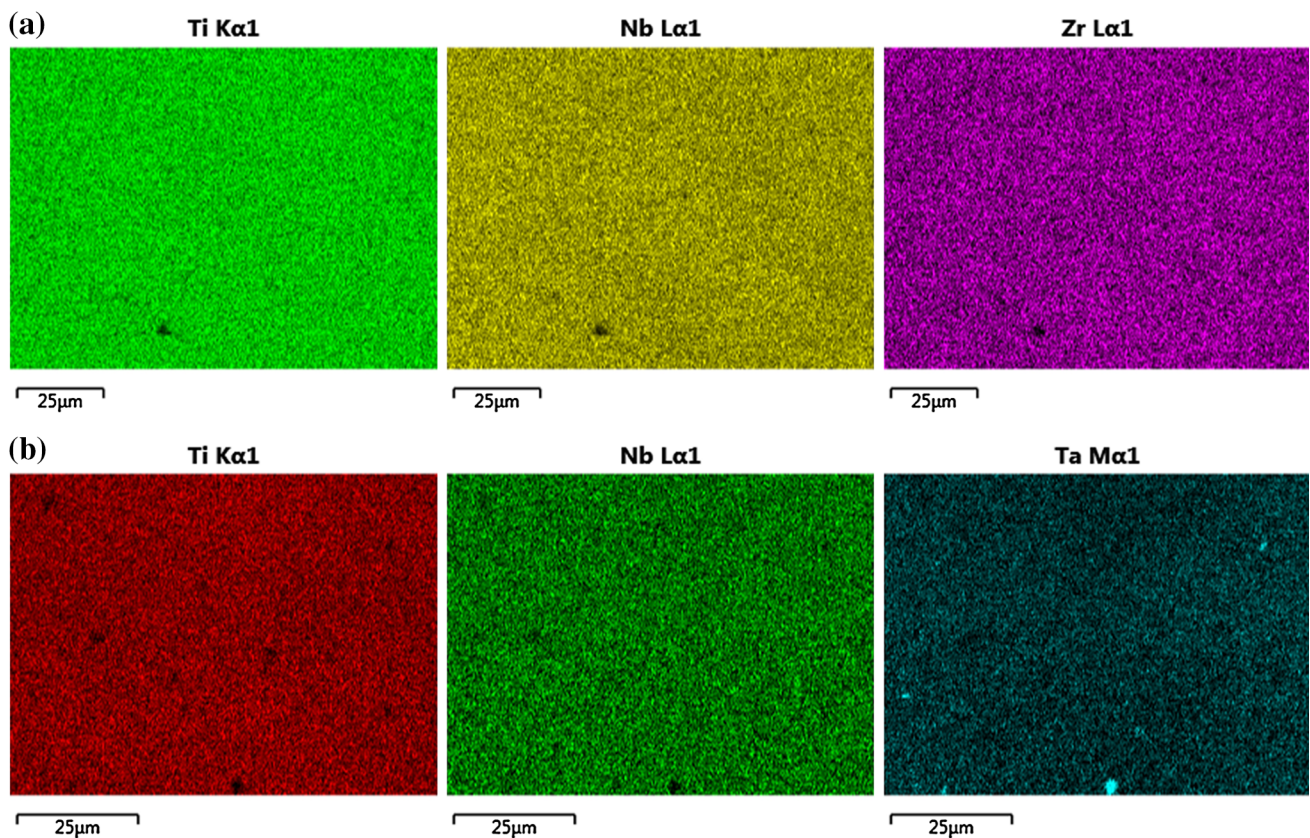
Fig. 1 SEM element distribution maps for **a** Ti–22Nb–6Zr and **b** Ti–22Nb–6Ta

Fig. 2 Cross section of a medium size ingot after first remelting (target composition Ti–22Nb–6Ta)

step, the elements' distribution was already homogeneous (Fig. 4), and the actual composition was close to that of the target Ti–22.1Nb–5.8Zr alloy.

TMT-Induced Structure Formation and Superelastic Behavior

Since the functional and mechanical properties of the studied alloys are strongly structure sensitive, they can be controlled by forming favorable microstructures in the material. The most common way to control the structural state of Ti-based SMA is to subject them to TMT, which generally comprises cold deformation and PDA, and may also involve additional age-hardening.

Structure Formation

A moderate cold deformation ($e = 0.3$–0.37) of the Ti–Nb–Zr and Ti–Nb–Ta alloys causes the formation of a well-developed dislocation substructure in the β-phase matrix and in the $\alpha(\alpha'')$-phase plates; deformation bands and ω-phase (in Ti–Nb–Zr alloy) can also be observed [8, 43, 44]. Contrarily to the Ti–Ni-based SMAs, an increase in the plastic deformation intensity up to $e \sim 2$ does not lead to amorphization of Ti–Nb-based alloys and to the formation in them of a predominant nanocrystalline structure after annealing [8, 44]. In this study therefore, the cold plastic deformation intensities are limited to their moderate
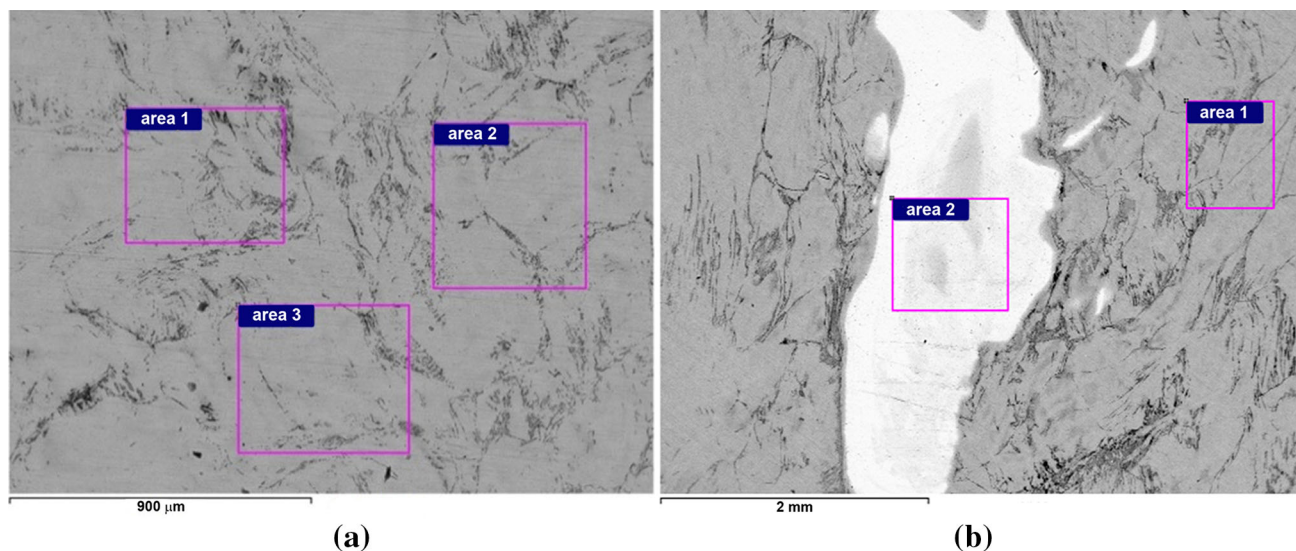
Fig. 3 SEM images of bottom (**a**) and top (**b**) zones of the ingot (target composition Ti–22Nb–6Ta); "area" *frames* indicate the fields for chemical analysis

Table 1 Average chemical composition of the lower and upper parts of the medium size ingot (target composition Ti–22Nb–6Ta)

Location within the ingot	Composition of the main elements (at.%)		
Zones	Ti	Nb	Ta
Bottom	74.1	24.7	1.3
Top, matrix	73.7	24.9	1.4
Top, inclusion	64.7	24.2	11.1

levels. Since annealing of undeformed Ti–Nb–Zr and Ti–Nb–Ta alloys does not significantly change their grain structure, annealing is only used in combination with cold deformation.

After PDA at 450 °C (60 min) of both alloys, no significant changes in the dislocation substructure of the β- and α-phases are observed; the density of dislocations remains high, and the general view of the structure is preserved, but an increase in the ω-phase content is observed in Ti–Nb–Zr alloy [43, 44, 51]. After PDA at 500 °C (60 min), a polygonized dislocation substructure

forms, which may be deduced from the limited azimuthal broadening of the diffraction spots in SAED patterns (Fig. 5a–c) indicating the absence of high-angle misorientations of β-phase. The observed structure is nanosubgrained with subgrain sizes ranging from 20 to 100 nm.

When the PDA temperature rises to 550 °C (60 min), the subgrains grow and cross the borderline between the nanometer and the submicrometer dimension (an average subgrain size is ∼100 nm, Fig. 5a). When the PDA temperature increases further (600 °C), but the annealing time remains relatively short (30 min for Ti–Nb–Zr and 15 min for Ti–Nb–Ta), a limited broadening of the β-phase X-ray reflections (Fig. 5b, c) indicates that low-angle misorientations are still preserved and the structure is still nanosubgrained.

After PDA at 600 °C (60 min), the size of the subgrains increases to submicrometer scale (200–500 nm), while some recrystallized β-phase grains up to a few microns in size can also be observed. After PDA at 750 °C, the β-phase structure is already recrystallized with a grain size of about 20 μm [44].
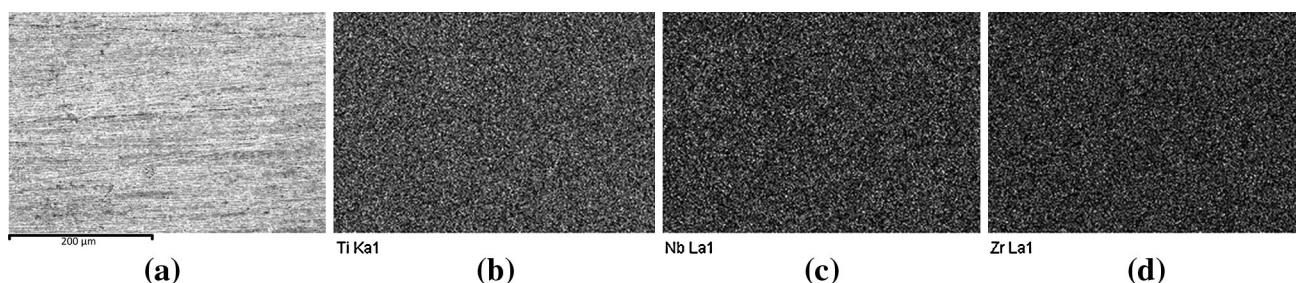

Fig. 4 Typical SEM image (**a**) and element distribution maps (**b–d**) in a medium size ingot (target composition Ti–22Nb–6Zr)
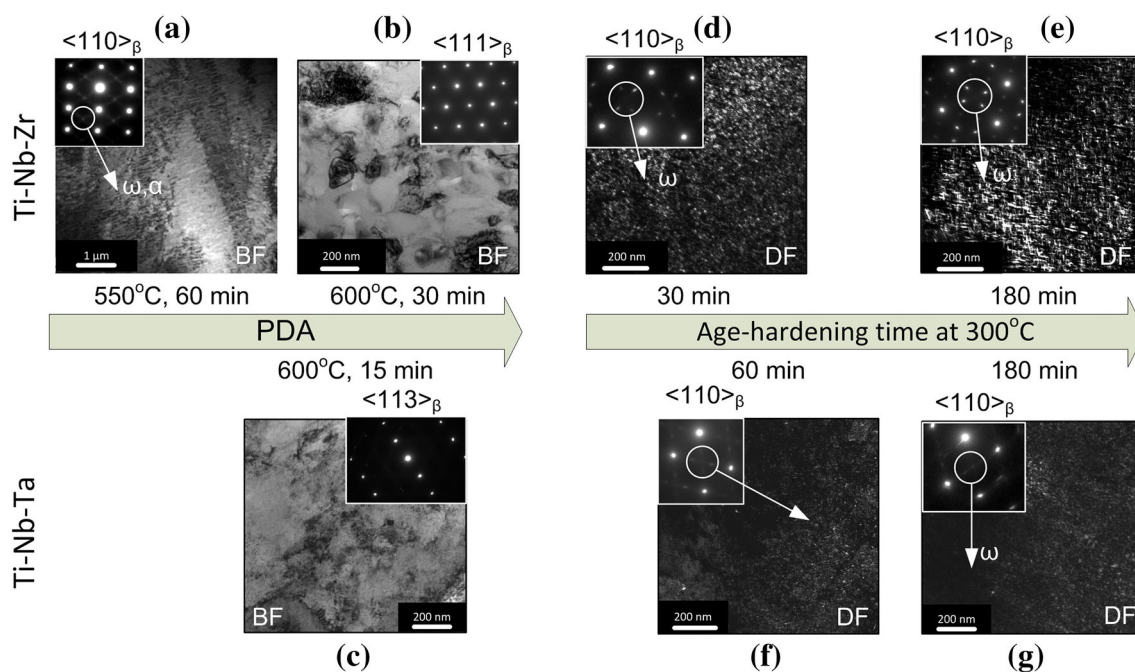
Fig. 5 TEM of structure evolution in Ti–21.8Nb–6Zr (**a**, **b**, **d**, **e**) and Ti–19.7Nb–5.8Ta (**c**, **f**, **g**) alloys under post-deformation annealing (**a**–**c**) and additional age-hardening (**d**–**g**)

Up to PDA at 550 °C, small quantities of ω-phase can still be found in the Ti–Nb–Zr alloy (after PDA at 600 °C, ω-phase reflections are no longer visible). In this alloy, small quantities of α-phase can be found throughout the 450,…,600 °C temperature range. In the Ti–Nb–Ta alloy, ω-phase cannot be distinctly detected by TEM irrespective of the PDA temperature; X-ray diffractograms of this alloy show small quantities of α(α′)-phase after PDA at 500 and 750 °C [47].

Age-hardening of both alloys at 300 °C results in the formation of nanosized (less than 10 nm) randomly scattered spherical ω-precipitates (Fig. 5d–g) [47–50]. After 30 min of age-hardening, ω-phase reflections are already clearly visible in micro-diffraction patterns of both alloys. The ω-phase particles are much finer and sparser in the Ti–Nb–Ta (Fig. 5f, g) than in the Ti–Nb–Zr (Fig. 5d, e) alloy. In the Ti–Nb–Ta alloy, ω-phase reflections are slightly visible on SAED patterns even after 180 min of age-hardening.

Superelastic Behavior

Cold deformation increases the strength, but drastically decreases the ductility of Ti–Nb–Zr and Ti–Nb–Ta alloys [8, 46]. Annealing of as-received Ti–Nb–Zr and Ti–Nb–Ta alloys does not bring their fatigue performance to an admissible level (number of cycles to failure is under a threshold of 100 cycles) [8, 46]. It appears evident that TMT is mandatory to improve the functional properties of these alloys.

When Ti–Nb–Zr alloy is subjected to CR ($e = 0.37$), 2 % strain fatigue life manifests a distinct maximum after PDA at 600 °C for 30 min ($N_{max} = 878$, Fig. 6a). During cycling, superelastic stress–strain loops are well-pronounced, Young's modulus is ∼40 GPa (first cycle), and reduces down to 25 GPa during cycling. Furthermore, the accumulation rate of residual strain after this TMT is the lowest [46]. Age-hardening of this alloy (300 °C, 10 min) significantly shortens its fatigue life ($N_{max} = 562$, see Fig. 6a).

Comparing the evolution of the Ti–Nb–Zr alloy microstructure with that of its mechanical behavior allows the conclusion that the maximum number of cycles to failure and the most perfect superelastic behavior correspond to the formation in this alloys of a nanosubgrained structure of β-phase (Fig. 5b). On the contrary, in this alloy system, ω-phase precipitation during age-hardening is an almost uncontrollable process, which leads to the formation of a significant quantity of ω-phase and to alloy embrittlement, even after a very short (as low as 10 min) age-hardening.

The Ti–Nb–Ta alloy subjected to CR ($e = 0.37$) + PDA 400 °C (60 min) shows interesting fatigue performances with a number of cycles to failure $N_{max} = 285$ (Fig. 6b).

Instead of selecting this TMT as a prerequisite treatment for subsequent age-hardening, PDA at a higher temperature (600 °C), but for a shorter period of time (15 min), was deemed more suitable, even though this last TMT led to a significantly shorter fatigue life ($N_{max} = 48$). (The rationale for this selection was that after PDA at 400 °C, the
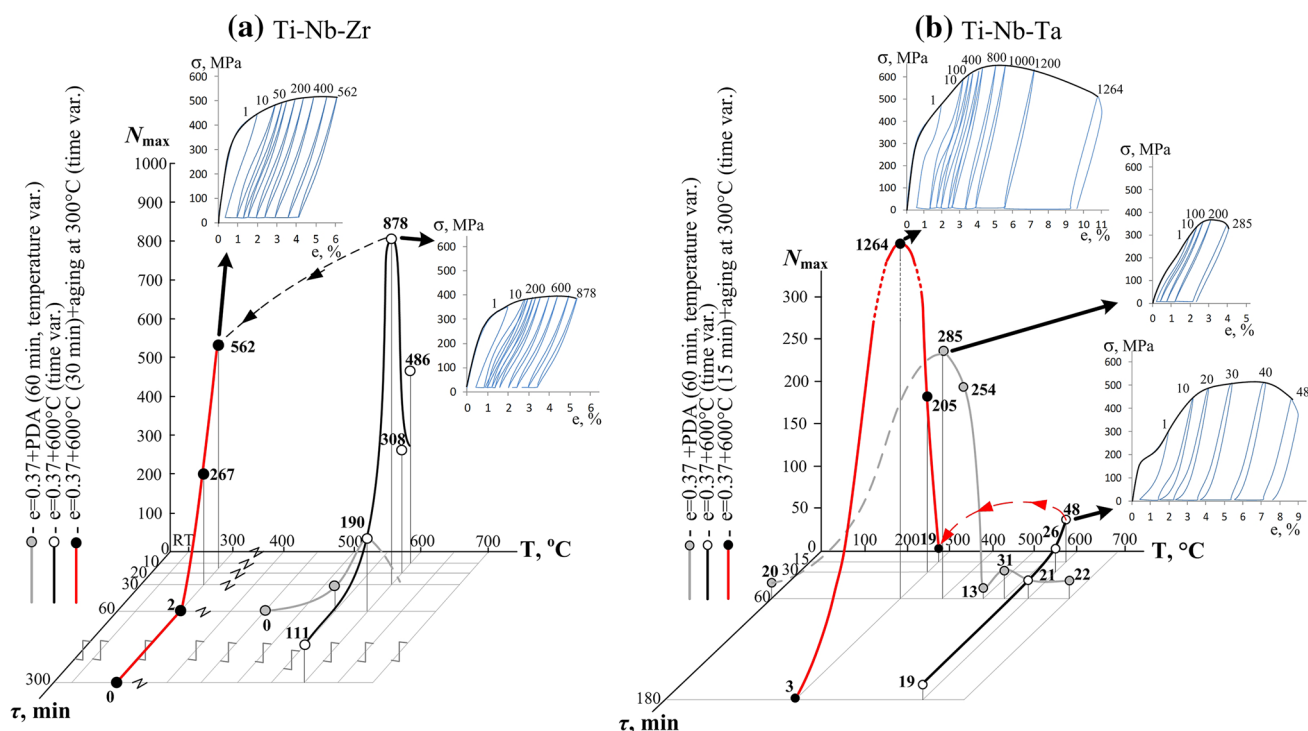
Fig. 6 Number of cycles to failure N_{max} of the Ti–21.8Nb–6Zr (**a**) and Ti–19.7Nb–5.8Ta (**b**) alloys during mechanocycling after various TMT routes with stress–strain curves in some key points

dislocation density in this alloy was still too high, which would limit the strengthening effect of age-hardening.)

Figure 6b shows that age-hardening at 300 °C (60 min) after PDA at 600 °C (15 min), effectively improves the alloy's fatigue resistance ($N_{max} = 1264$). This treatment has a tag price of a relatively higher Young's modulus (60 GPa), but leads to an almost perfect superelastic behavior and smallest residual strain accumulation during cycling, as compared to other TMT routes. Such an improved superelastic behavior is a direct result of a controllable ω-phase precipitation during aging of the nanosubgrained Ti–Nb–Ta alloy.

Based on the obtained results, the following TMT routes can be regarded as optimum for the realization of a perfect multi-cycle superelastic behavior in the studied alloys: Ti–Nb–Zr-CR ($e = 0.37$) + PDA (600 °C, 30 min), and Ti–Nb–Ta-CR ($e = 0.37$) + PDA (600 °C, 15 min) + AG (300 °C, 60 min).

Functional Stability and Fatigue Resistance of Thermomechanically Treated Ti–Nb-Based SMAs

Long-Term Stability Tests

Bone implants are intended for prolonged use, perceiving variable cyclic loads in an aggressive environment of the human body. Increasing the service life of implant materials and improving the stability of their functional properties are important challenges faced by the modern biomaterial science. In the light of that, studies examining the stability of their mechanical behavior during multi-cycle functional tests, as well as during long-term isothermal exposures, are important.

In this work, Ti–21.8Nb–6Zr and Ti–19.7Nb–5.8Ta alloys were subjected to TMT to create different microstructures. The evolutions of their superelastic behavior were monitored during mechanical "loading-unloading" 2 % strain 10-cycle testing (three times) and during long-term pauses between testing (40 and 365 days).

Three series of functional 10-cycle tests with intermediate 40- and 365-day pauses were performed to assess the long-term stability of the superelastic behavior of Ti–Nb–Ta and Ti–Nb–Zr SMAs. The evolution of the loading–unloading stress–strain diagrams during superelastic cycling, after RT pauses and repeated superelastic cycling is presented in Fig. 7, while the evolution of the characteristic parameters of the diagrams is illustrated in Fig. 8. Both alloys manifest non-perfect superelastic behavior during the first testing cycles, which rapidly evolves towards perfect superelasticity [52, 53].

For both alloys, the initial values of their "engineering" Young's moduli are close (30–40 GPa). These values decrease to 20–25 GPa during the first series of

mechanocycling, with the one exception being Ti–Nb–Ta after aging (Fig. 8a, b). After a 40-day RT pause, the Young's moduli regain their initial values and start to decrease again during the second cycling series, but this time, much less rapidly. Finally, after a 365-day RT pause, the Young's moduli of both alloys regain their initial values and remain stable during the final cycling run. The Ti–Nb–Zr alloy, especially after PDA at 600 °C (30 min) shows a slight increase in accumulated strain during superelastic cycling (Fig. 8a, b). In the case of Ti–Nb–Ta, the accumulated strain increases more rapidly.

For both alloys, their transformation yield stresses (σ_{tr}) decrease during cycling and regain their initial values after the pauses (Fig. 8c, d). The Ti–Nb–Ta alloy demonstrates a specific feature: the 365-day RT pause leads to a significant increase in the transformation yield stress as compared to its pre-testing values (Fig. 8c). A maximum stress reached within a single loading–unloading cycle (σ_{max}) increases during all testing sequences and decreases to its almost initial value after RT pauses (Fig. 8c, d). An increasing difference ($\sigma_{max} - \sigma_{tr}$) results in an improvement of the superelastic behavior, preventing earlier involvement of the unrecoverable plastic deformation in the deformation process [1, 2, 4, 5].

It can be concluded that the Ti–Nb–Zr alloy with an initial nanosubgrained structure after PDA at 600 °C (30 min) demonstrates the most perfect and stable low-modulus superelastic behavior as compared to Ti–Nb–Ta alloy, thus revealing its better biomechanical compatibility.

Functional Fatigue Tests

The mechanocycling tests described above were performed by applying a constant strain of $\varepsilon_c = 2$ % in each cycle. As a result, the TMT routes leading to the longest functional fatigue life were determined. However, for prospective medical applications of these materials (bone implants), the cyclic strain magnitude rarely exceeds 0.2 % [54]. To investigate their functional fatigue behavior under conditions mimicking real applications, the Ti–Nb–Zr alloy exhibiting the most stable functional behavior with different TMT-induced microstructures was fatigue tested under cycling strains ranging from a low-level apparently elastic strain ($\varepsilon_c = 0.2$ %) to a high-level superelastic strain ($\varepsilon_c = 1.5$ %) [55].

The main result of the functional fatigue testing is the number of cycles to failure. It can be observed on the Wôhler-type diagram of Fig. 9 that the higher the strain magnitude, the shorter the fatigue life. For the smallest strain magnitude ($\varepsilon_c = 0.2$ %), the longest fatigue life (run-out without failure at 1×10^6 cycles) is observed after PDA at 450 °C (60 min). For the same strain magnitude, the number of cycles to failure after PDA at 600 °C (30 min) is lower ($\sim 5 \times 10^5$). When the strain magnitude increases to $\varepsilon_c = 0.3$ %, the number of cycles to failure after PDA at 450 and 600 °C are the same ($\sim 3.5 \times 10^4$). For any strain above 0.3 %, the fatigue life after PDA at 600 °C becomes longer than that after 450 °C, and the higher the strain, the greater the advantage of the 600 °C-annealed specimens. After PDA at 750 °C (30 min), the fatigue life is the shortest for all of the applied strains.
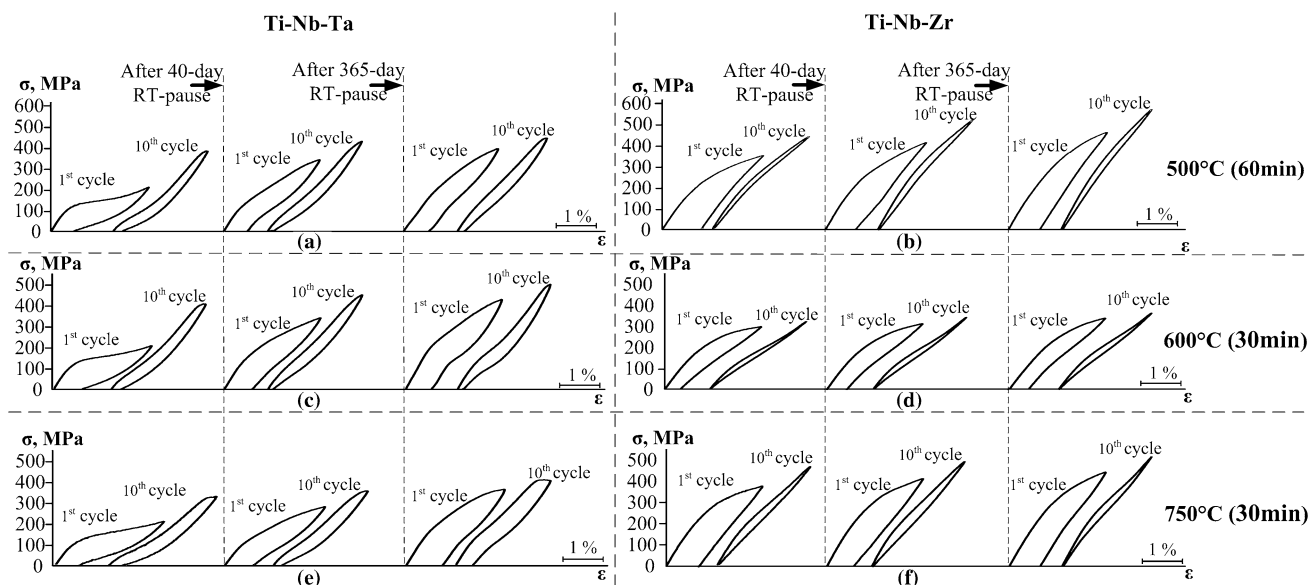

Fig. 7 Evolution of loading–unloading diagrams of the a, c, e Ti–19.7Nb–5.8Ta and b, d, f Ti–21.8Nb–6Zr alloys during multi-cycle tests after PDA at a, b 500 °C, c, d 600 °C and e, f 750 °C
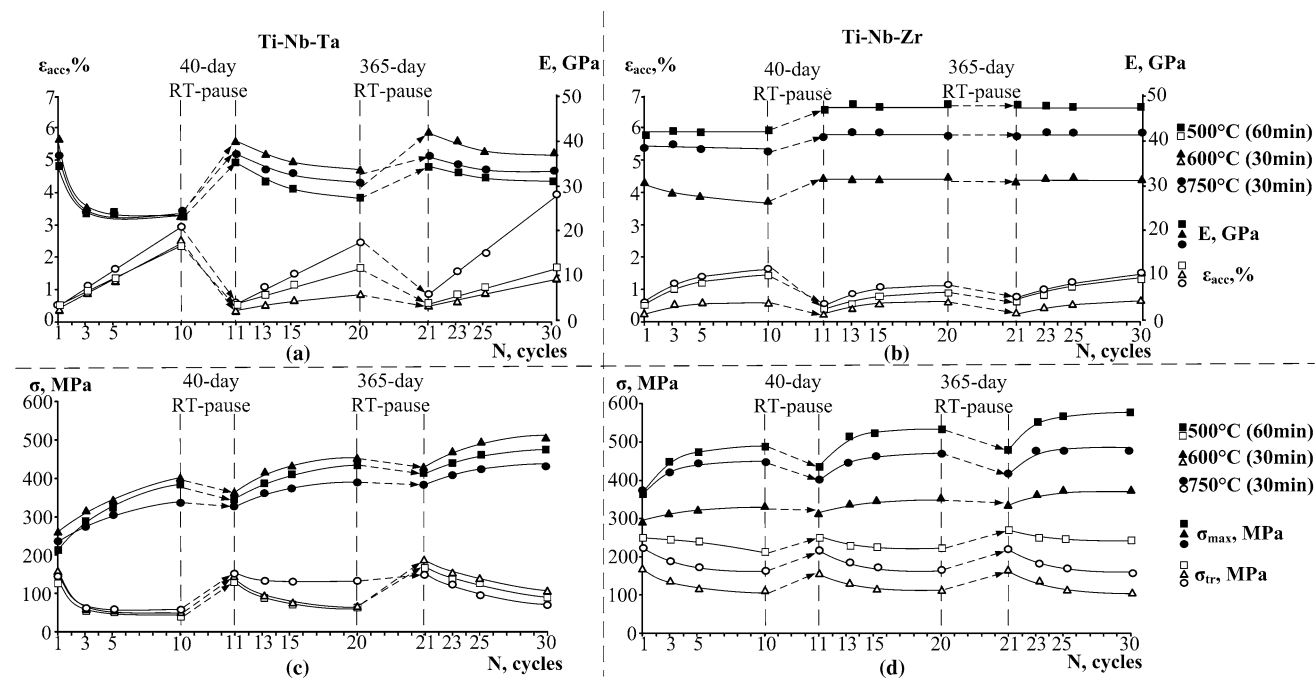
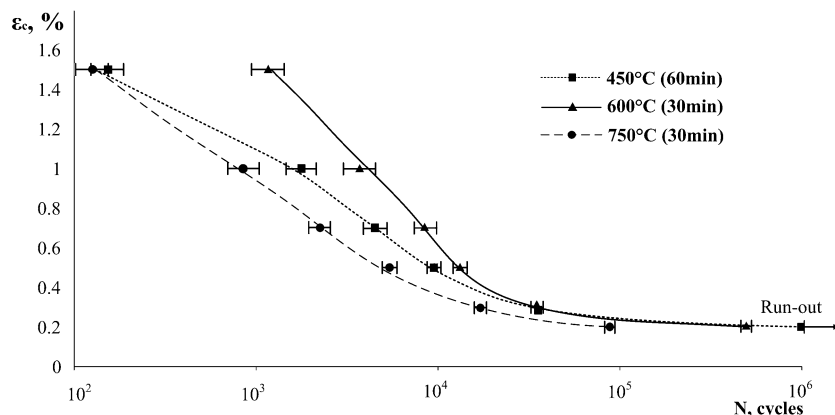**Fig. 8** Evolution of loading–unloading diagram parameters: **a**, **c** Ti–19.7Nb–5.8Ta, **b**, **d** Ti–21.8Nb–6Zr, **a**, **b** Young's modulus and accumulated strain, and **c**, **d** maximum stress attained in a cycle and transformation yield stress

Fig. 9 Number of cycles to failure versus strain magnitude of the Ti–21.8Nb–6Zr alloy

As can be observed in Fig. 10, which shows the evolution of functional fatigue parameters during mechanocycling, the pre-test values of the Young's modulus are not the same after different PDA: 55 GPa (PDA at 450 °C), 40 GPa (600 °C), and 50 GPa (750 °C). During low-strain cycling (0.2 %), these values are stable. Cycling with higher strains results in the Young's modulus decrease. This phenomenon is inherent to the superelastic cycling behavior and reflects the gradually increasing involvement of the superelasticity mechanism in the deformation process [48, 55]. The lower the PDA temperature, the more hardened the material, and the higher the strain when this evolution becomes clearly observable.

In all cases, except for the 1.5 % strain cycling, the lowest accumulated strain is observed after PDA at 450 °C (Fig. 10f). For 1.5 % strain testing, the lowest accumulated strain during cycling corresponds to PDA at 600 °C (Fig. 10f). The lowest accumulated strain is an obvious consequence of a more complete involvement of the superelasticity mechanisms in the deformation process. The evolution of the superelastic behavior during cycling is most visible for the 600 and 750 °C cases when the cyclic strain exceeds 0.7 % (Fig. 10c). The highest cyclic stresses σ_{max} are observed for the 450 °C-annealed specimens, and the higher the strain magnitude, the greater the difference between the maximum cyclic transformation yield stress as

the latter decreases with an increase in the number of cycles (Fig. 10c, d, f).

Corrosion and Electrochemical Behavior

As the implants, while in service, contact corrosive biological media of the human body, it is of a great practical interest to study the corrosion and electrochemical behavior of the Ti–Nb-based alloys in physiological solutions, including the case of cyclic load application. Some selected results of these studies [56–60] are described below.

Open Circuit Potential (OCP), Polarization Diagrams, Corrosion Rate

The character of OCP evolution under exposure to simulated solutions is an important tool for studies of tendency to passivation and regularities of the protective film formation on the alloy surface. Figure 11 compares OCP curves of the Ti–Nb–Ta, Ti–Nb–Zr, commercially pure Ti (cp-Ti), and Ti–Ni in Hank's solution at 37 °C [51]. Figure 12 shows the polarization diagrams of these alloys.

The corrosion rate calculated from the results of weight loss measurements during prolonged corrosion immersion testing in Hank's solution is 1.2×10^{-3} mm/year (Ti–Nb–Ta), 2.3×10^{-3} mm/year (Ti–Nb–Zr), 1.9×10^{-3} mm/year (cp-Ti), 1.4×10^{-3} mm/year (Ti–Ni).

The concentration of Ti (<0.005 mg/l), Nb (<0.01 mg/l), Ta (<0.05 mg/l), and Zr (<0.001 mg/l) ions in the test solution is below detection level; however, Ni concentration can be measured (0.022 mg/l).
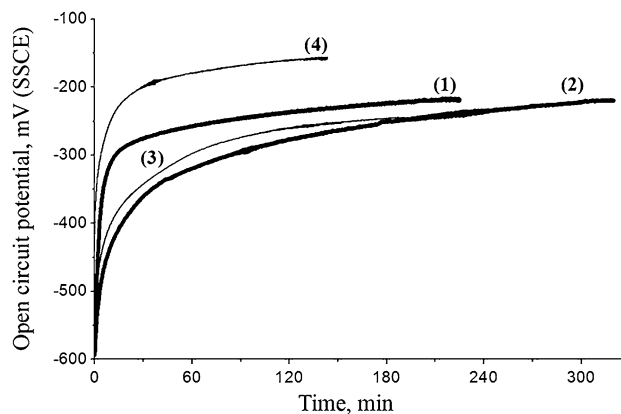

Fig. 11 OCP curves of Ti–22Nb–6Ta (*1*), Ti–22Nb–6Zr (*2*) alloys, cp-Ti (*3*), and Ti–50.9Ni (*4*) in Hank's solution at 37 °C [51, 58]

Mechanocyclic Tests in Simulated Physiological Solutions

The results of OCP measurements during mechanocycling tests of the Ti–Nb–Ta alloy in Hank's solution are presented in Fig. 13 [51]. The number of cycles to failure is about 8800 for Ti–Nb–Ta at 1.0 % strain. Note that the same testing routine is applied to the Ti–Nb–Zr alloy, with a significantly lower number of cycles to failure of 3300 [51].

In Vitro Cell Compatibility

Table 2 lists the results of the fibroblast growth activity and viability investigation after a 1-day incubation using the MTT method. Optical density values which are within a
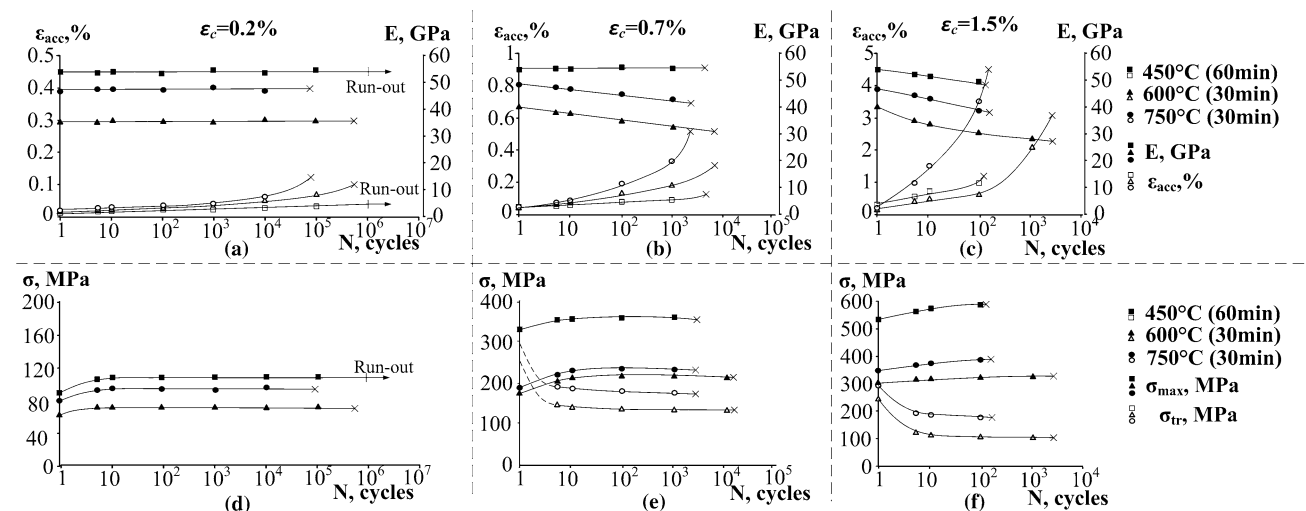

Fig. 10 Evolution of loading–unloading diagram parameters: **a–c** Young's modulus and accumulated strain, and **d–f** maximum stress attained in a cycle and transformation yield stress
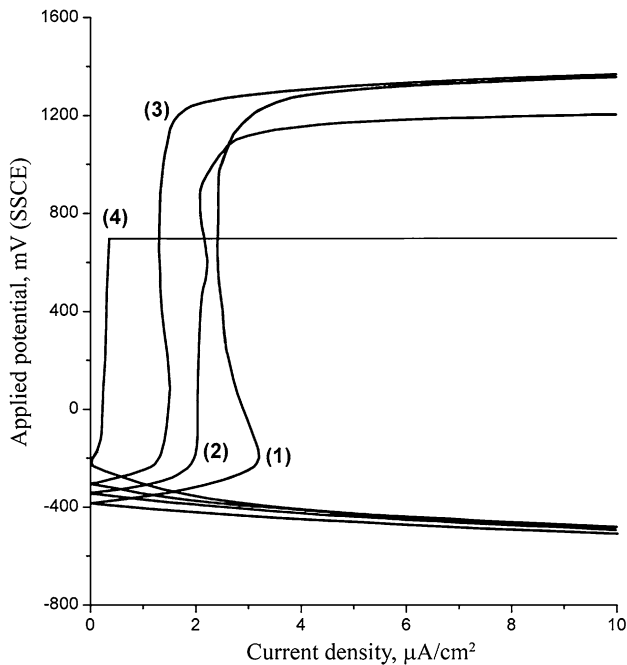
Fig. 12 Polarization diagrams (potential sweep rate 0.1 mV/s) for Ti–22Nb–6Ta, Ti–22Nb–6Zr, cp-Ti, and Ti–50.9Ni alloys at 37 °C in Hank's solution
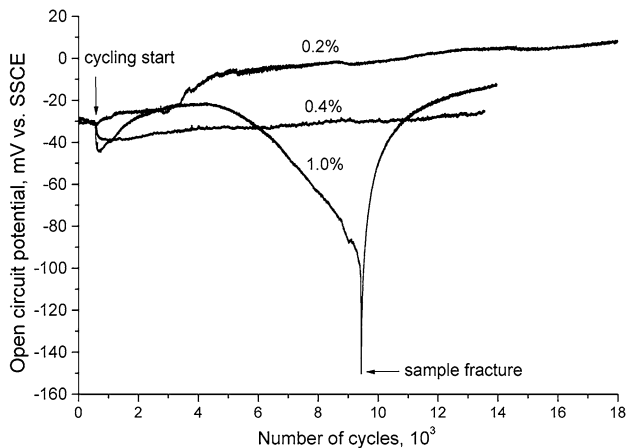

Fig. 13 OCP curves of Ti–22Nb–6Ta under cyclic load in Hank's solution at 37 °C with various strain values

20 % deviation limit from the cell control sample can be considered as non-toxic for the cells. The parameters of fibroblasts cultured for 4 days on Ti–Nb–Zr, Ti–Nb–Ta, and reference materials are presented in Table 3.

A comparison of the parameters from Table 3 shows that the Ti–Nb–Zr alloy show a higher cell survival rate than the Ti–Nb–Ta alloy after prolonged cell cultivation.

Discussion

Based on the results of investigations presented above, the following general comments can be formulated:

Regarding the manufacturing aspects, three remelting steps are required to produce homogeneous ingots of the Ti–Nb–Zr alloy by the VAM method. Due to the high melting point of Ta, Ti–Nb–Ta alloys are more difficult to produce: it takes at least four remelting steps to obtain ingots of acceptable quality. It is also very important to carry out preparatory melting in the presence of Ti sponge getters to reduce a risk of contamination during melting. Note that the use of preliminary smelted Nb–Ta alloy as a foundry alloy is strongly recommended for smelting medium and large size Ti–Nb–Ta ingots.

The structure changes with CR strain in the $e = 0.3$–2 range in Ti–Nb solid solution-based alloys differ from the well-studied processes in intermetallic Ti–Ni SMAs. This difference is in the form of an absence of structure amorphization even after severe CR with a true strain as high as $e = 2$ [29, 44–46, 51]. As a consequence, 500–550 °C (60 min) annealing of such severely deformed Ti–Nb alloys results in the formation of a mixed nanosubgrained and nanocrystalline structure of β-phase [44, 51]. The superelastic fatigue life of these alloys turns out to be much shorter than that of their moderately deformed ($e = 0.3$–0.37) counterparts with a nanosubgrained structure after the same annealing conditions [44–46].

The structure evolution in Ti–21.8Nb–6Zr and Ti–19.7Nb–5.8Ta alloys subjected to TMT with CR ($e = 0.3$–0.37) and PDA (400,…,750 °C, 60 min) follows the common phases of β-phase recovery, polygonization (including subgrain formation and growth), and recrystallization. The subgrain size of the polygonized dislocation substructure remains in the nanometer dimension after 60 min PDA below 600 °C or 30 min PDA at 600 °C for both alloys. The primary recrystallization in the polygonized substructure starts after PDA at 600 °C, and after PDA at 700 °C, the β-phase is completely recrystallized [44]. These processes are somewhat delayed in the Ta-

Table 2 Results of fibroblast growth activity and viability investigation after incubation for 1 day using MTT method

Samples	Optical density at 545 nm	Difference from the control (%)
Cell control	0.692 ± 0.071	0
Ti–Nb–Ta	0.619 ± 0.011	−11
Ti–Nb–Zr	0.679 ± 0.016	−2
Ti–Ni	0.657 ± 0.070	−5

Table 3 Parameters of fibroblasts cultured for 4 days with the Ti–Nb-based and Ti–Ni alloys

Samples	Scepter Millipore pipette data			
	Average volume (pl)	Average diameter (μm)	Concentration (cell/ml, 10^4)	Deviation of cell concentration (%)
Cell control	3.38	18.63	6.78	0
Ti–Nb–Ta	1.45	14.06	6.96	+3
Ti–Nb–Zr	2.44	16.71	9.64	+42
Ti–Ni	2.65	17.18	7.64	+13

doped alloys because of the lower diffusion coefficient of Ta in the Ti–Nb matrix [44].

The formation of ω-phase precipitates is observed in the β-phase of the TMT-processed nanosubgrained Ti–Nb–Zr and Ti–Nb–Ta alloys during aging at 300 °C. The Ti–Nb–Zr alloy is characterized by a much higher precipitation rate of nanosized ω-phase particles as compared to the Ti–Nb–Ta alloy. This is because tantalum is a more effective inhibitor of the isothermal ω-phase formation than zirconium.

PDA in the 500–600 °C temperature range yields minimum values of Young's modulus, transformation yield stress, and ultimate tensile strength. For the Ti–Nb–Ta alloy, the best combination of functional fatigue properties corresponds to either a well-developed, but partially recovered, dislocation substructure of β-phase, or to an optimally precipitation-hardened nanosubgrained structure. The first structure is obtained after CR ($e = 0.37$) + PDA (400/450 °C, 60 min) processing route, while the second structure is obtained after the CR ($e = 0.37$) + PDA (600 °C, 15 min) + AG (300 °C, 60 min) processing route. Much slower kinetics of ω-phase precipitation in Ti–Nb–Ta, compared to Ti–Nb–Zr, allows the optimization of the degree of precipitation hardening, which leads to a drastic increase in the alloy's fatigue resistance.

For Ti–Nb–Zr, the best combination of functional properties corresponds to a nanosubgrained structure formation in β-phase as a result of the CR ($e = 0.37$) + PDA (600 °C, 30 min) processing route, without additional aging. The aging of this alloy for even short periods of time (min) leads to its excessive dispersion hardening (overaging), and, therefore, to the alloy's brittleness; the latter combined with a concomitant decrease in the M_s temperature, leads to a drastic degradation of the alloy's functional performances.

In the functional stability experiments on the Ti–Nb–Zr and Ti–Nb–Ta alloys, all superelastic functional parameters change extensively as a result of the first 2 % strain 10-cycle cycling routine. The Young's modulus, residual strain in a cycle, and transformation yield stress rapidly decrease, while the maximum stress in the cycle and accumulated strain increase at different rates. For both alloys, the 40-day RT pause leads to an almost complete restoration of the initial superelastic loading–unloading behavior, and then, during the second 10-cycle testing series, this behavior evolves again, but to a lesser extent. The subsequent 365-day RT pause and the third testing series do not affect the superelastic behavior markedly. The significant superelastic characteristic variations during the first, second, and third series of superelastic cycling are caused by the intense accumulation and subsequent "saturation" of the oriented residual stresses and substructural hardening.

The strain-controlled fatigue life of the Ti–22Nb–6Zr alloy under strains ranging from apparently elastic to superelastic is strongly dependent on the alloy's microstructure. The longest fatigue life of the alloy in the apparently elastic strain range ($\varepsilon_c = 0.2$ %) is shown by the highly dislocated and the most strain-hardened material (PDA at 450 °C, 60 min) possessing the true elastic yield stress. In the superelastic strain range ($\varepsilon_c > 0.3$ %), the advantage in the functional fatigue life goes to the material with the polygonized (nanosubgrained) dislocation substructure (PDA at 600 °C, 30 min). This advantage increases as the maximum strain per cycle increases up to $\varepsilon_c = 1.5$ %, indicating the much higher reliability of the last structure in the case of occasional overloading during service. The involvement of the reversible β ↔ α″ stress-induced phase transformation and the corresponding effect of superelasticity results in an overall improvement of the fatigue resistance of metastable near-beta Ti–Nb–Zr alloys, as compared to their elasto-plastically deformed counterparts.

Over the entire long-term experiment, Ti–Nb–Zr demonstrates more stable and clearly identified superelastic behavior than Ti–Nb–Ta; this is especially true for the nanostructured material (PDA at 600 °C, 30 min), when the Young's modulus reaches an ultra-low value of 30 GPa. A combination of highly biocompatible alloy components, high elongation to failure, adequate static and dynamic

functional properties with exceptionally low Young's modulus gives the nanosubgrained superelastic Ti–22Nb–6Zr alloy high biomechanical compatibility and makes it highly suitable for orthopedic implants, in a wide range of loading–unloading conditions, from apparently elastic to superelastic applied strains.

Superelastic Ti–Nb-based SMA exhibit a tendency of self-passivation in Hank's simulated physiological solution. The process of protective film formation during exposure in these media may be described by two logarithmic equations, indicating different mechanisms of formation and growth of the films at different stages. The alloys undergo corrosion at a low rate (about 10^{-3} mm/year) and are practically as good in terms of corrosion–electrochemical characteristics as titanium and titanium nickelide. Moreover, they manifest superelasticity, as opposed to titanium; contain no carcinogenic components, and are not subjected to pitting corrosion unlike titanium nickelide.

The OCP measurements of the alloys carried out in Hank's solution with applied strain values ranging from 0.2 to 1.0 % show that at clinically relevant strain values (about 0.2 %), the alloys exhibit OCP growth indicating their high stability and resistance to corrosion fatigue under these cycling conditions. At much higher strains (1 %), fatigue crack initiation and propagation take place; however, the corresponding OCP variation indicates that the fracture process is significantly restrained by reversible martensitic transformation during cycling.

The results of the investigation of fibroblast growth activity and viability investigation after incubation for 24 h using the MTT method show that all the studied superelastic alloys do not exhibit toxicity to human fibroblast cells, with the Ti–Nb–Zr alloy performing slightly better than the Ti–Nb–Ta alloy. Moreover, the Ti–Nb–Zr alloy shows significantly higher cell survival rate than the Ti–Nb–Ta alloy after prolonged cell cultivation (+42 % compared to +13 % after a 4-day test).

Presently, the authors concentrate their efforts on thermomechanical processing of multi-component Ti–Zr-based alloys. As shown in the works of Miyazaki, Kim et al. [39–41], these alloys are advanced Ni-free materials possessing significantly higher superelastic recovery strain limits than Ti–Nb-based SMAs. The main idea is to use a combination of titanium, zirconium, niobium, and tantalum to improve the suitability of these alloys for biomedical applications through the optimization of their PDA and age-hardening schedules.

Appendix

Melting Point Estimation for Ti–Nb–Ta and Ti–Nb–Zr Alloys

The equation of liquidus surface for Ti–Nb–Ta and Ti–Nb–Zr ternary phase diagrams was obtained from the combination of the liquidus lines in the corresponding phase equilibrium binary diagrams. Since these binary diagrams do not feature eutectic transformation or intermetallics lines, the liquidus surfaces for the ternary systems can be considered as smooth.

The calculation was performed using *OriginLab Origin 8.0* software non-linear surface fit function:

$$T = \frac{T_0 + a_{01}(C_{Nb}) + b_{01}(C_2) + b_{02}(C_2)^2 + b_{03}(C_2)^3}{1 + a_1(C_{Nb}) + a_2(C_{Nb})^2 + a_3(C_{Nb})^3 + b_1(C_2) + b_2(C_2)^2}, \quad (1)$$

where T is temperature (°C), T_0 is in number equal to the melting point of pure titanium, C_{Nb} is Nb concentration (at.%), C_2 is the concentration of the second alloying element (Ta or Zr, at.%), a_{01}, a_1, a_2, a_3, b_{01}, b_{02}, b_{03}, b_1, b_2 are coefficients.

Taking into account all statistically significant coefficients in Eq. (1) one can obtain the following equations (correlation coefficients R^2 are given in brackets):

Ti–Nb–Ta:

$$T = \frac{1667 + 5(C_{Nb}) + 40(C_{Ta}) - 0.23(C_{Ta})^2}{1 + 0.010(C_{Ta})}$$
$$(R^2 = 0.999),$$

$$T = \frac{1667 + 40(C_{Nb}) - 40(C_{Zr}) + 0.41(C_{Zr})^2}{1 + 0.024(C_{Nb}) - 0.22(C_{Zr})}$$
$$(R^2 = 1.000).$$

According to these dependences, the melting point of Ti–22Nb–6Ta and Ti–22Nb–6Zr (at.%) alloys accounts to 1877 ± 30 and 1710 ± 51 °C, respectively (assuming element content error 0.5 at.%).

References

1. Funakubo H (1987) Shape memory alloys. Gordon and Breach, New York
2. Duerig TW, Melton KN, Stockel D, Wayman CM (1990) Engineering aspects of shape memory alloys. Butterworth-Heinemann, London
3. Monasevich LA (1992) Shape memory effects and their application in medicine. Nauka, Novosibirsk
4. Otsuka K, Wayman CM (1998) Shape memory materials. Cambridge University Press, Cambridge

5. Brailovski V, Prokoshkin S, Terriault P, Trochu F (2003) Shape memory alloys: fundamentals, modeling and applications. ETS Publishers, Montreal

6. Prokoshkin SD, Pushin VG, Ryklina EP, Khmelevskaya IY (2004) Application of titanium nickelide-based alloys in medicine. Phys Met Metallogr 97(1):56–96

7. Yoneyama T, Miyazaki S (2009) Shape memory alloys for biomedical applications. Woodhead Publishers, Cambridge

8. Resnina N, Rubanik V (2015) Shape memory alloys: properties, technologies, opportunities. Trans Tech Publications, Pfaffikon

9. Miyazaki S, Otsuka K, Suzuki Y (1981) Transformation pseudoelasticity and deformation behavior in Ti–50.6 at% Ni. Scr Metall 15:287–292

10. Prokoshkin SD, Kaputkina LM, Bondareva SA (1991) Structure of hot-deformed austenite and properties of Ti–Ni–Fe alloy after HTMT. Phys Met Metallogr 70(3):144–149

11. Prokoshkin SD, Kaputkina LM, Morozova TV, Khmelevskaya IY (1995) Dilatometric anomalies and shape memory effect in titanium–nickel alloy subjected to low-temperature thermomechanical treatment. Phys Met Metallogr 80(3):277–282

12. Prokoshkin SD, Kaputkina LM, Khmelevskaya IY, Morozova TV (1995) Martensitic transformations and shape memory effect in thermomechanically treated Ti–Ni alloys. J Phys IV 5:563–568

13. Treppmann D, Hornbogen E, Wurzel D (1995) The effect of combined recrystallization and precipitation processes on the functional and structural properties in TiNi alloys. J Phys IV Col C8 Suppl J Phys III 5(12):569–574

14. Filip P, Rusek J, Mazanec K (1991) The effect of heat treatment on the structural stability of TiNi alloys. Z Metallkunde 82(6):488–491

15. Sittner P, Yokoun D, Dayananda GN, Stalmans R (2000) Recovery stress generation in shape memory Ti$_{50}$Ni$_{45}$Cu$_5$ thin wires. Mater Sci Eng A 286:298–311

16. Khmelevskaya IY, Prokoshkin SD, Shipsha VG, Bazhenov IP, Ryklina EP (2002) Thermomechanical strengthening of titanium nickelide and structure changes upon generation and forced isothermal relaxation of reactive stress. Phys Met Metallogr 93(2):189–195

17. Brailovski V, Khmelevskaya IY, Prokoshkin SD, Pushin VG, Ryklina EP, Valiev RZ (2004) Foundations of heat and thermomechanical treatments and their effect on the structure and properties of titanium-nickelide based alloys. Phys Met Metallogr 97(1):3–55

18. Prokoshkin S, Brailovski V, Khmelevskaya I, Dobatkin S, Inaekyan K, Turilina V, Demers V, Tatyanin E (2005) Creation of substructure and nanostructure by thermomechanical treatment and control of functional properties of Ti–Ni alloys with shape memory effect. Met Sci Heat Treat 47(5–6):182–187

19. Brailovski V, Prokoshkin S, Khmelevskaya I, Inaekyan K, Demers V, Dobatkin S, Tatyanin E (2006) Structure and properties of the Ti–50.0 at% Ni alloy after strain hardening and nanocrystallizing thermomechanical processing. Mater Trans 47(3):795–804

20. Prokoshkin S, Brailovski V, Inaekyan K, Demers V, Khmelevskaya I, Dobatkin S, Tatyanin E (2008) Structure and properties of severely cold-rolled and annealed Ti–Ni shape memory alloys. Mater Sci Eng A 481–482:114–118

21. Khmelevskaya IYu, Prokoshkin SD, Trubitsyna IB, Belousov MN, Dobatkin SV, Tatyanin EV, Korotitskiy AV, Brailovski V, Stolyarov VV, Prokofiev EA (2008) Structure and properties of Ti–Ni-based alloys after equal-channel angular pressing and high-pressure torsion. Mater Sci Eng A 481–482:119–122

22. Demers V, Brailovski V, Prokoshkin S, Inaekyan K (2009) Thermomechanical fatigue of nanostructured Ti–Ni shape memory alloys. Mater Sci Eng A 513–514:185–196

23. Brailovski V, Prokoshkin S, Inaekyan K, Demers V (2011) Functional properties of nanocrystalline, submicrocrystalline and polygonized Ti–Ni alloys processed by cold rolling and post-deformation annealing. J Alloy Compd 509(5):2066–2075

24. Delville R, Malard B, Pilch J, Sittner P, Delville R, Schryvers D (2010) Microstructure changes during non-conventional heat treatment of thin Ni–Ti wires by pulsed electric current studied by transmission electron microscopy. Acta Mater 58:4503–4515

25. Young ML, Wagner MF-X, Frenzel J, Schmahl WW, Eggeler G (2010) Phase volume fractions and strain measurements in an ultrafine-grained NiTi shape-memory alloy during tensile loading. Acta Mater 58:2344–2354

26. Malard B, Pilch J, Sittner P, Delville R, Curfs C (2011) In situ investigation of the fast microstructure evolution during electropulse heat treatment of cold drawn NiTi wires. Acta Mater 59:1542–1556

27. Kreitcberg A, Brailovski V, Prokoshkin S, Inaekyan K, Facchinello Y, Dubinskiy S (2013) Microstructure and functional fatigue of nanostructured Ti–50.26 at% Ni alloy after thermomechanical treatment with warm rolling and intermediate annealing. Mater Sci Eng A 562:118–127

28. Kreitcberg AYu, Prokoshkin SD, Brailovski V, Korotitskiy AV (2014) Role of the structure and texture in the realization of the recovery strain resource of the nanostructured Ti–50.26 at % Ni alloy. Phys Met Metallogr 115(9):926–947

29. Prokoshkin S, Brailovski V, Inaekyan K, Korotitskiy A, Kreitcberg A (2015) Thermomechanical treatment of TiNi intermetallic-based shape memory alloys. Mater Sci Found 81–82:260–341

30. Prokoshkin S, Brailovski V, Inaekyan K, Demers V, Kreitcberg A (2015) Nanostructured Ti–Ni shape memory alloys produced by thermomechanical processing. Shape Mem Superelast 1(2):191–203

31. Miyazaki S, Kim HY, Hosoda H (2006) Development and characterization of Ni-free Ti-based shape memory and superelastic alloys. Mater Sci Eng A 438–440:18–24

32. Kim JI, Kim HY, Inamura T, Hosoda H, Miyazaki S (2005) Shape memory characteristics of Ti–22Nb–(2–8)Zr (at%) biomedical alloys. Mater Sci Eng A 403:334–339

33. Kim HY, Hashimoto S, Kim JI, Inamura T, Hosoda H, Miyazaki S (2006) Effect of Ta addition on shape memory behavior of Ti–22Nb alloy. Mater Sci Eng A 417:120–128

34. Niinomi M (2008) Mechanical biocompatibilities of titanium alloys for biomedical applications. J Mech Behav Biomed Mater 1:30–42

35. Hao YI, Niinomi M, Kuroda D, Fukunaga K, Zhou YI, Yang R, Suzuki A (2003) Aging response of the Young's modulus and mechanical properties of Ti–29Nb–13Ta–4.6Zr alloy for biomedical applications. Metall Mater Trans A 34:1007–1012

36. Li Q, Niinomi M, Nakai M, Cui Z, Zhu S, Yang X (2012) Effect of Zr on superelasticity and mechanical properties of Ti–24 at% Nb–(0, 2, 4) at% Zr alloy subjected to aging treatment. Mater Sci Eng A 536:197–206

37. Akahori T, Niinomi M, Fukui H, Suzuki A (2004) Fatigue, fretting fatigue and corrosion characteristics of biocompatible beta type titanium alloy conducted with various thermomechanical treatment. Mater Trans 45:1540–1548

38. Laheurte P, Prima F, Eberhardt A, Gloriant T, Wary M, Patoor E (2010) Mechanical properties of low modulus β titanium alloys designed from electronic approach. J Mech Behav Biomed Mater 3:565–573

39. Fu J, Yamamoto A, Kim HY, Hosoda H, Miyazaki S (2015) Novel Ti-base superelastic alloys with large recovery strain and excellent biocompatibility. Acta Biomater 17:56–67

40. Kim HY, Fu J, Tobe H, Kim JI, Miyazaki S (2015) Crystal structure, transformation strain and superelastic property of Ti–Nb–Zr and Ti–Nb–Ta alloys. Shape Mem Superelast 1:107–116

41. Ijaz MF, Kim HY, Hosoda H, Miyazaki S (2015) Superelastic properties of biomedical (Ti–Zr)–Mo–Sn alloys. Mater Sci Eng C 48:11–20

42. Pavon LL, Kim HY, Hosoda H, Miyazaki S (2015) Effect of Nb content and heat treatment on superelastic properties of Ti–24Zr–(8–12)Nb–2Sn. Scr Mater 95:46–49

43. Brailovski V, Prokoshkin S, Gauthier M, Inaekyan K, Dubinskiy S, Petrzhik M, Filonov M (2011) Bulk and porous metastable beta Ti–Nb–Zr(Ta) alloys for biomedical applications. Mater Sci Eng C 31:643–657

44. Dubinskiy SM, Prokoshkin SD, Brailovski V, Korotitskiy AV, Inaekyan KE, Filonov MR, Petrzhik MI (2011) Structure formation during thermomechanical processing of Ti–Nb–Zr(Ta) alloys and manifestation of the shape-memory effect. Phys Met Metallogr 112(5):529–542

45. Brailovski V, Prokoshkin S, Inaekyan K, Dubinskiy S, Gauthier M (2012) Mechanical properties of thermomechanically processed metastable beta Ti–Nb–Zr alloys for biomedical applications. Mater Sci Forum 706–709:455–460

46. Prokoshkin S, Brailovski V, Korotitskiy A, Inaekyan K, Dubinskiy S, Filonov M, Petrzhik M (2013) Formation of nanostructures in thermomechanically treated Ti–Ni and Ti–Nb–(Zr, Ta) SMAs and their roles in martensite crystal lattice changes and mechanical behavior. J Alloy Compd 577(1):418–422

47. Dubinskiy S, Brailovski V, Prokoshkin S, Pushin V, Inaekyan K, Sheremetyev V, Petrzhik M, Filonov M (2013) Structure and properties of Ti–19.7Nb–5.8Ta shape memory alloy subjected to thermomechanical processing including aging. J Mater Eng Perform 22(9):2656–2664

48. Prokoshkin S, Brailovski V, Petrzhik M, Filonov M, Sheremetyev V (2013) Mechanocyclic and time stability of loading–unloading diagram parameters of nanostructured Ti–Nb–Ta and Ti–Nb–Zr SMA. Mater Sci Forum 738–739:481–485

49. Brailovski V, Prokoshkin S, Inaekyan K, Dubinskiy S (2013) Influence of omega-phase precipitation hardening on the static and dynamic properties of metastable beta Ti–Nb–Zr and Ti–Nb–Ta alloys. Mater Sci Forum 738–739:189–194

50. Inaekyan K, Brailovski V, Prokoshkin S, Pushin V, Dubinskiy S, Sheremetyev V (2015) Comparative study of structure formation and mechanical behavior of age-hardened Ti–Nb–Zr and Ti–Nb–Ta shape memory alloys. Mater Charact 103:65–74

51. Brailovski V, Prokoshkin S, Inaekyan K, Petrzhik M, Filonov M, Pustov Y, Dubinskiy S, Zhukova Y, Korotitskiy A, Sheremetyev V (2015) Thermomechanical treatment of Ti–Nb solid solution based SMA. Mater Sci Found 81–82:342–405

52. Sheremetyev VA, Prokoshkin SD, Brailovski V, Dubinskiy SM, Korotitskiy AV, Filonov MR, Petrzhik MI (2015) Investigation of the structure stability and superelastic behavior of thermomechanically treated Ti–Nb–Zr and Ti–Nb–Ta shape memory alloys. Phys Met Metallogr 116(4):413–422

53. Sheremetyev V, Prokoshkin S, Brailovski V, Dubinskiy S, Filonov M, Petrzhik M (2015) Long-term stability of superelastic behavior of nanosubgrained Ti–Nb–Zr and Ti–Nb–Ta shape memory alloys. Mater Today Proc 2S:S26–S31

54. Mavcic B, Antonic V (2012) Optimal mechanical environment of the healing bone fracture/osteotomy. Int Orthop 36:689–695

55. Sheremetyev V, Brailovski V, Prokoshkin S, Inaekyan K, Dubinskiy S (2016) Functional fatigue behavior of superelastic beta Ti–22Nb–6Zr (at%) alloy for load-bearing biomedical applications. Mater Sci Eng C 58:935–944

56. Zhukova YuS, Pustov YuA, Konopatsky AS, Filonov MR (2014) Characterization of electrochemical behavior and surface oxide films on superelastic biomedical Ti–Nb–Ta alloy in simulated physiological solutions. J Alloy Compd 586:535–538

57. Zhukova YuS, Pustov YuA, Konopatsky AS, Filonov MR, Prokoshkin SD (2014) Electrochemical behavior of novel superelastic biomedical alloys in simulated physiological media under cyclic load. J Mater Eng Perform 23(7):2677–2681

58. Zhukova YS, Pustov YA, Konopatsky AS, Dubinskiy SM, Filonov MR, Brailovski V (2015) Corrosion fatigue and electrochemical behavior of superelastic Ti–Nb–Ta alloy for medical implants under cyclic load conditions. Mater Today Proc 2S:S991–S994

59. Zhukova YuS, Pustov YuA, Filonov MR (2012) Kinetic regularities and mechanism of formation of nanosize passive films on titanium alloys for medical application and their electrochemical behavior in simulated physiological media. Prot Met Phys Chem Surf 48:315–321

60. Pustov YuA, Zhukova YuS, Filonov MR (2014) The role of martensitic transformation in corrosion fatigue failure of Ti–22 Nb–6 Ta and Ti–22 Nb–6 Zr (at%) medical alloys. Prot Met Phys Chem Surf 50:524–529